

$\bar{b}c$ susceptibilities from fully relativistic lattice QCDJudd Harrison^{*}*SUPA, School of Physics and Astronomy, University of Glasgow, Glasgow, G12 8QQ, United Kingdom*

(Received 2 July 2024; accepted 19 August 2024; published 10 September 2024)

We compute the $\bar{h}c$ (pseudo)scalar, (axial-)vector and (axial-)tensor susceptibilities as a function of $u = m_c/m_h$ between $u = m_c/m_b$ and $u = 0.8$ using fully relativistic lattice QCD, employing non-perturbative current renormalization and using the second generation $2 + 1 + 1$ MILC HISQ gluon field configurations. We include ensembles with $a \approx 0.09, 0.06, 0.045,$ and 0.033 fm and we are able to reach the physical b -quark on the two finest ensembles. At the physical $m_h = m_b$ point we find $\bar{m}_b^2 \chi_{1^+} = 0.720(34) \times 10^{-2}$, $\bar{m}_b^2 \chi_{1^-} = 1.161(54) \times 10^{-2}$, $\chi_{0^-} = 2.374(33) \times 10^{-2}$, and $\chi_{0^+} = 0.609(14) \times 10^{-2}$. Our results for the (pseudo)scalar, vector, and axial vector are compatible with the expected small size of nonperturbative effects at $u = m_c/m_b$. We also give the first nonperturbative determination of the tensor susceptibilities, finding $\bar{m}_b^2 \chi_T = 0.891(44) \times 10^{-2}$ and $\bar{m}_b^2 \chi_{AT} = 0.441(33) \times 10^{-2}$. Our value of $\bar{m}_b^2 \chi_{AT}$ is in good agreement with the $\mathcal{O}(\alpha_s)$ perturbation theory, while our result for $\bar{m}_b^2 \chi_T$ is in tension with the $\mathcal{O}(\alpha_s)$ perturbation theory at the level of 2σ . These results will allow for dispersively bounded parametrizations to be employed using lattice inputs for the full set of $h \rightarrow c$ semileptonic form factors in future calculations, for heavy-quark masses in the range $1.25 \times m_c \leq m_h \leq m_b$.

DOI: [10.1103/PhysRevD.110.054506](https://doi.org/10.1103/PhysRevD.110.054506)**I. INTRODUCTION**

Lattice QCD studies of the semileptonic decays of $B_{(s,c)}$ mesons to vector mesons via the $b \rightarrow c \ell \bar{\nu}$ weak transition have progressed significantly in recent years, with lattice form factor results becoming available away from zero recoil for $B \rightarrow D^* \ell \bar{\nu}$ [1–3], $B_s \rightarrow D_s^{(*)} \ell \bar{\nu}$ [4,5], and $B_c \rightarrow J/\psi \ell \bar{\nu}$ [6]. However, lattice predictions for the differential decay rate for $B \rightarrow D^* \ell \bar{\nu}$ have been found to be in tension with that measured by the Belle experiment [7]. Moreover, predictions for the ratios of form factors obtained by combining earlier zero-recoil lattice results with light-cone sum rules (LCSR) and QCD sum rules (QCDSR) using the heavy-quark expansion (HQE) through order $\mathcal{O}(1/m_b, 1/m_c^2)$ [8] show some disagreement with the more recent lattice-only results.

For fully relativistic lattice calculations, it is typical to compute form factors at multiple heavy-quark masses, m_h , below and ranging up to m_b , in order to control discretization effects appearing as powers of $(am_h)^2$ [2–6]. The lattice data is then fit using a function chosen to describe both the physical heavy mass dependence and kinematics,

as well as discretization and quark mass mistuning effects. The choice of this fit function is one potential origin of the discrepancy seen between lattice-only results and the results combining LCSR, zero-recoil lattice and HQE for $B \rightarrow D^*$.

In the continuum, the $B \rightarrow D^{(*)}$ form factors obey dispersive bounds and may be described using the Boyd-Grinstein-Lebed (BGL) parametrization [9], which we briefly describe below. This parametrization is formulated using the variable

$$z(q^2, t_+, t_0) = \frac{\sqrt{t_+ - q^2} - \sqrt{t_+ - t_0}}{\sqrt{t_+ - q^2} + \sqrt{t_+ - t_0}}, \quad (1)$$

where t_+ is the $\bar{b}c$ two particle production threshold for the relevant current and t_0 is a free parameter which may be chosen between t_+ and $-\infty$. z maps the physical q^2 region to within the unit circle and the branch cut $q^2 \geq t_+$ to the unit circle. The susceptibilities, χ_{J^P} , are defined in terms of the two point correlation functions of $\bar{b}c$ currents with quantum numbers J^P (see Sec. II), and are typically computed using perturbation theory. The susceptibilities can then be related via the optical theorem and crossing symmetry to a sum over the squared magnitudes of exclusive hadronic matrix elements. Because each contribution in this sum is positive semidefinite, the sum may be restricted to just the lowest two particle contribution, corresponding to $B \rightarrow D^{(*)}$. This results in inequalities involving the helicity-basis form factors, F , integrated over

*Contact author: judd.harrison@glasgow.ac.uk

Published by the American Physical Society under the terms of the [Creative Commons Attribution 4.0 International license](https://creativecommons.org/licenses/by/4.0/). Further distribution of this work must maintain attribution to the author(s) and the published article's title, journal citation, and DOI. Funded by SCOAP³.

the unit circle in z . These inequalities take the form

$$\int_C |P(z)\phi(z)F(z)|^2 \leq 1, \quad (2)$$

where $\phi(z)$, referred to as outer functions, are analytic functions on the open unit disk, which also absorb a factor of $1/\sqrt{\chi_{J^P}}$ in order to set the right-hand side of Eq. (2) to unity. The Blaschke factors, $P(z)$, have magnitude 1 on the unit circle, and remove subthreshold poles appearing in the form factor. $P(z)\phi(z)F(z)$ can then be analytically continued to real z corresponding to the physical semileptonic region of q^2 . Because $P(z)\phi(z)F(z)$ is analytic on the open unit disc, it may be expanded as a polynomial in z as

$$P(z)\phi(z)F(z) = \sum_{n=0}^{\infty} a_n z^n, \quad (3)$$

resulting in the standard BGL parametrization for the form factor,

$$F(z) = \frac{1}{P(z)\phi(z)} \sum_{n=0}^{\infty} a_n z^n, \quad (4)$$

where from Eq. (2) the coefficients satisfy the inequality

$$\sum_{n=0}^{\infty} |a_n|^2 \leq 1. \quad (5)$$

Note that stronger dispersive bounds than those of the original BGL approach may be formulated by decomposing the polarization tensor for a given current in terms of a full set of virtual vector boson polarization vectors [10]. Also note that the BGL parametrization corresponds to the special case where the lowest two particle threshold, t_+ , corresponds to the production threshold, t_Γ , of the initial and final state mesons for the form factors of interest. In the more general case where $t_\Gamma \geq t_+$, the integral in Eq. (2) is restricted to an arc on the unit circle, and instead of a simple sum of powers of z as in Eq. (4), one finds a sum over polynomials in z constructed to be orthonormal on the corresponding arc [10].

On the lattice, the HPQCD Collaboration has previously employed two different fit functions to reach the physical continuum. Earlier works on $B_s \rightarrow D_s^*$ and $B_c \rightarrow J/\psi$ used a ‘‘pseudo-BGL’’ fit [4,6], where a power series in the conformal variable z was used to describe the kinematic dependence of the form factors in the QCD basis, together with a term describing the $\bar{b}c$ subthreshold poles. However, these fits omitted the outer functions of the full BGL parametrization Eq. (4). More recently, for a combined analysis of $B \rightarrow D^*$ and $B_s \rightarrow D_s^*$, the HPQCD Collaboration used a fit to the HQET form factors using a simple power series in $w-1$, choosing priors to ensure the continuum BGL coefficients were not significantly

constrained relative to the unitarity bounds [2]. In both cases, coefficients included $(\Lambda/m_h)^i$ corrections encoding the physical heavy mass dependence.

Neither of these fit functions is ideal. The pseudo-BGL fit neglects the dependence on the heavy-quark mass of the outer functions, as well as losing the ability to choose prior widths informed by the unitarity constraints. On the other hand, the HQET fit includes limited information about the known pole structure of the form factors with varying heavy quark mass. Ideally a full BGL fit would be used to fit lattice data, augmenting the BGL coefficients with Λ/m_h terms to describe the dependence of the lattice data on heavy-quark mass while using lattice inputs to describe the subthreshold pole masses and susceptibilities. This approach is complicated by the susceptibilities, which determine the overall normalization of the outer functions [9]. The susceptibilities for the $\bar{b}c$ (pseudo)scalar and (axial-)vector currents are known perturbatively for the physical b -quark to three loops [11,12], with nonperturbative condensate contributions expected to be extremely small. These susceptibilities have also recently been computed nonperturbatively using lattice QCD [13], where surprising tension at the level of $\approx 2\sigma$ was found between the lattice and perturbation theory at the $m_h = m_b$ point. The tension is particularly surprising because of the good consistency seen between the continuum perturbation theory and the equivalent heavyonium quantities [14,15].

Recently, lattice form factor calculations have also been extended to include the tensor form factors needed to analyze and constrain new physics [2,16]. Dispersive parametrizations of the tensor form factors require tensor susceptibilities computed from the polarization tensor of the corresponding tensor currents. For $\bar{b}c$ currents, these are currently only available from perturbation theory to $\mathcal{O}(\alpha_s)$ [17].

In this work, we compute the full set of (pseudo)scalar, (axial-)vector, and (axial-)tensor susceptibilities as a function of $u = m_c/m_h$ between $u^{\text{phys}} = m_c/m_b$ and ≈ 0.8 using the $a \approx 0.09, 0.06, 0.045,$ and 0.03 fm second generation MILC HISQ $2+1+1$ gauge field ensembles. This will provide an additional check of the perturbation theory and lattice results [13] for the (pseudo)scalar and (axial-)vector susceptibilities, as well as providing new lattice results for the $\bar{b}c$ (axial-)tensor susceptibilities. These new (axial-)tensor susceptibilities will allow future heavy-HISQ calculations of form factors for exclusive $b \rightarrow c$ processes to use the full dispersive parametrization for all form factors, while using lattice results for all inputs. This calculation will also lead to a future calculation of the heavy-light susceptibilities, where nonperturbative condensate contributions are expected to be more sizeable.

II. THEORETICAL BACKGROUND

A. (Pseudo)scalar and (axial-)vector currents

The susceptibilities are related to polarization functions, which are decomposed according to Lorentz structure, and

are defined in terms of current-current correlators by

$$\begin{aligned} & (-q^2 g_{\mu\nu} + q_\mu q_\nu) \Pi^\delta(q^2) + q_\mu q_\nu \Pi_L^\delta(q^2) \\ & = i \int dx e^{iqx} \langle 0 | T j_\mu^\delta(x) j_\nu^{\delta\dagger}(0) | 0 \rangle, \end{aligned} \quad (6)$$

for the vector and axial-vector currents $j_\mu^V = \bar{\psi}_h \gamma_\mu \psi_c$, $j_\mu^A = \bar{\psi}_h \gamma_\mu \gamma^5 \psi_c$ and by

$$q^2 \Pi^\delta(q^2) = i \int dx^4 e^{iqx} \langle 0 | T j^\delta(x) j^{\delta\dagger}(0) | 0 \rangle, \quad (7)$$

for the scalar and pseudoscalar currents $j^S = \bar{\psi}_h \psi_c$ and $j^P = i \bar{\psi}_h \gamma^5 \psi_c$. Moments of the heavy-light current correlators were computed up to three loops in perturbation theory in [11,12] in the $\overline{\text{MS}}$ scheme. The three-loop $\overline{\text{MS}}$ results for the limit $q^2 \rightarrow 0$ are expressed as

$$\bar{\Pi}^\delta(q^2) = \frac{3}{16\pi^2} \sum_{n \geq -1} \bar{C}_n^\delta(u) z^n \quad (8)$$

where $u = m_c/m_h$ and $z = q^2/m_h^2$. The susceptibilities are then defined at the point $q^2 = 0$ by

$$\begin{aligned} \chi_{1+}(q^2 = 0) & \equiv \frac{1}{2} \frac{\partial^2}{\partial^2 q^2} (q^2 \Pi^A(q^2))|_{q^2=0}, \\ \chi_{1-}(q^2 = 0) & \equiv \frac{1}{2} \frac{\partial^2}{\partial^2 q^2} (q^2 \Pi^V(q^2))|_{q^2=0}, \\ \chi_{0-}(q^2 = 0) & \equiv \frac{(m_h + m_c)^2}{2} \frac{\partial^2}{\partial^2 q^2} (q^2 \Pi^P(q^2))|_{q^2=0}, \\ \chi_{0+}(q^2 = 0) & \equiv \frac{(m_h - m_c)^2}{2} \frac{\partial^2}{\partial^2 q^2} (q^2 \Pi^S(q^2))|_{q^2=0}, \end{aligned} \quad (9)$$

where in the final two lines we have used the partially conserved axial-vector and vector current relations. Inserting Eq. (8) into Eq. (9) gives the susceptibilities in terms of the perturbatively computed moments of [11,12] as

$$\begin{aligned} \chi_{1+}(q^2 = 0) & = \frac{3}{\bar{m}_h^2 16\pi^2} \bar{C}_1^A(u), \\ \chi_{1-}(q^2 = 0) & = \frac{3}{\bar{m}_h^2 16\pi^2} \bar{C}_1^V(u), \\ \chi_{0-}(q^2 = 0) & = (1+u)^2 \frac{3}{16\pi^2} \bar{C}_1^P(u), \\ \chi_{0+}(q^2 = 0) & = (1-u)^2 \frac{3}{16\pi^2} \bar{C}_1^S(u), \end{aligned} \quad (10)$$

where the \bar{C}_1^δ are given by [11,12]

$$\bar{C}_1^\delta(u) = \bar{C}_1^{(0),\delta}(u) + \frac{\alpha_s}{\pi} \bar{C}_1^{(1),\delta}(u) + \left(\frac{\alpha_s}{\pi}\right)^2 \bar{C}_1^{(2),\delta}(u) \quad (11)$$

with $\alpha_s = \alpha_s(\mu)$ and $\mu = \bar{m}_h(\bar{m}_h)$. Note that Eq. (11) does not include nonperturbative condensate contributions. To set \bar{m}_h we use $\bar{m}_c(3 \text{ GeV}) = 0.9858(51) \text{ GeV}$ from [18] to compute $\bar{m}_h(3 \text{ GeV}) = \bar{m}_c(3 \text{ GeV})/u$, which we then run to $\bar{m}_h(\bar{m}_h)$. We use $\alpha_{\overline{\text{MS}}}(5 \text{ GeV}, n_f = 4) = 0.2128(25)$ from [15], together with the four-loop running [19]. We use $u^{\text{phys}} = 1/4.578(12)$ computed in pure QCD from [20]. We include an uncertainty for the three-loop result of $\sigma_3(\alpha_s/\pi)^3$ where σ_3 is the root mean square of $\bar{C}_1^{(0),\delta}(u)$, $\bar{C}_1^{(1),\delta}(u)$ and $\bar{C}_1^{(2),\delta}(u)$.

B. (Axial-)tensor currents

The susceptibilities are defined analogously for the tensor and axial-tensor currents, with one of the tensor indices contracted with q^α

$$j_\mu^T = \bar{\psi}_h \sigma_{\mu\alpha} q^\alpha \psi_c, \quad j_\mu^{AT} = \bar{\psi}_h \sigma_{\mu\alpha} \gamma^5 q^\alpha \psi_c. \quad (12)$$

The polarization functions for the (axial-)tensor currents given in Eq. (12) are defined by

$$\begin{aligned} (q_\mu q_\alpha - q^2 g_{\mu\alpha}) \Pi^T(q^2) & = i \int dx e^{iqx} \langle 0 | T j_\mu^T(x) j_\nu^{T\dagger}(0) | 0 \rangle, \\ (q_\mu q_\nu - q^2 g_{\mu\nu}) \Pi^{AT}(q^2) & = i \int dx e^{iqx} \langle 0 | T j_\mu^{AT}(x) j_\nu^{AT\dagger}(0) | 0 \rangle. \end{aligned} \quad (13)$$

Note that because $\sigma_{\mu\nu}$ is antisymmetric, there is no longitudinal piece proportional to the projector $q_\mu q_\nu/q^2$. The (axial-)tensor polarization functions require three subtractions [17], and the susceptibilities are defined by

$$\chi_{(A)T}^{J=1}(q^2 = 0) \equiv \frac{1}{6} \frac{\partial^3}{\partial^3 q^2} (q^2 \Pi^{(A)T}(q^2))|_{q^2=0}. \quad (14)$$

Since the $J = 0$ components of the polarization tensors are identically zero, we will omit the $J = 1$ label from the susceptibilities and write $\chi_{(A)T} \equiv \chi_{(A)T}^{J=1}$ from now on. The tensor currents also require renormalization in the continuum. This is typically performed in the $\overline{\text{MS}}$ scheme, and the tensor susceptibilities are dependent upon the renormalization scale μ .

III. LATTICE CALCULATION

Following [13], the continuum Euclidean correlation functions that we wish to compute are

TABLE I. Details of the gauge field configurations used in our calculation [22,23]. We use the Wilson flow parameter [24], w_0 , to fix the lattice spacing given in column 2. The physical value of w_0 was determined in [25] to be 0.1715(9) fm and the values of w_0/a , which are used together with w_0 to compute a , were taken from [15,18,26]. In these works, the unimproved Wilson flow was used in combination with the unimproved clover observable. Set 1 is referred to as “fine,” set 2 as “superfine,” set 3 as “ultrafine,” set 4 as “exafine,” and set 5 as “physical fine.” n_{cfg} is the number of configurations that we use here. am_{l0} , am_{s0} , and am_{c0} are the masses of the sea up/down, strange and charm quarks in lattice units. We also include the approximate mass of the Goldstone pion, computed in [27].

Set	a (fm)	w_0/a	$L_x \times L_t$	am_{l0}	am_{s0}	am_{c0}	M_π (MeV)	n_{cfg}
1	0.0902	1.9006(20)	32×96	0.0074	0.037	0.440	316	1000
2	0.0592	2.896(6)	48×144	0.0048	0.024	0.286	329	500
3	0.0441	3.892(12)	64×192	0.00316	0.0158	0.188	315	375
4	0.0327	5.243(16)	96×288	0.00223	0.01115	0.1316	309	100
5	0.0879	1.9518(7)	64×96	0.0012	0.0363	0.432	129	500

$$\begin{aligned}
C_A(t) &= \frac{Z_V^2}{3} \sum_{j=1}^3 \int dx^3 \langle 0 | T \bar{h} \gamma_j^E \gamma_5^E c(x) \bar{c} \gamma_j^E \gamma_5^E h(0) | 0 \rangle, & \chi_{1^+}(q^2=0) &= \frac{1}{12} \int dt t^4 C_A(t), \\
C_V(t) &= \frac{Z_V^2}{3} \sum_{j=1}^3 \int dx^3 \langle 0 | T \bar{h} \gamma_j^E c(x) \bar{c} \gamma_j^E h(0) | 0 \rangle, & \chi_{1^-}(q^2=0) &= \frac{1}{12} \int dt t^4 C_V(t), \\
C_P(t) &= \int dx^3 \langle 0 | T \bar{h} \gamma_5^E c(x) \bar{c} \gamma_5^E h(0) | 0 \rangle, & \chi_{0^-}(q^2=0) &= \frac{1}{12} (m_h + m_c)^2 \int dt t^4 C_P(t), \\
C_S(t) &= \int dx^3 \langle 0 | T \bar{h} c(x) \bar{c} h(0) | 0 \rangle, & \chi_{0^+}(q^2=0) &= \frac{1}{12} (m_h - m_c)^2 \int dt t^4 C_S(t), \\
C_T(t) &= \frac{Z_T^2}{3} \sum_{j=1}^3 \int dx^3 \langle 0 | T \bar{h} \sigma_{j0}^E c(x) \bar{c} \sigma_{j0}^E h(0) | 0 \rangle, & \chi_{(A)T}(q^2=0) &= \frac{1}{12} \int dt t^4 C_{(A)T}(t). \\
C_{AT}(t) &= \frac{Z_T^2}{3} \sum_{j=1}^3 \int dx^3 \langle 0 | T \bar{h} \sigma_{j0}^E \gamma_5^E c(x) \bar{c} \sigma_{j0}^E \gamma_5^E h(0) | 0 \rangle, & &
\end{aligned} \tag{15}$$

where γ_j^E and γ_5^E are Euclidean gamma matrices and for the (axial-)vector and (axial-)tensor currents we require the additional current renormalization factors Z_V and Z_T respectively.

Using the definitions of the susceptibilities, together with the definitions of the polarization functions, the susceptibilities may be expressed in terms of these correlation functions as [13]

We compute the required correlation functions using the HISQ [21] formalism for the h and c quarks on the MILC $2+1+1$ HISQ gluon field configurations detailed in Table I. We use the local spin-taste operators $1 \otimes 1$, $\gamma_5 \otimes \gamma_5$, $\gamma_j \otimes \gamma_j$ and $\gamma_j \gamma_5 \otimes \gamma_j \gamma_5$ for the S , P , V , and A currents respectively. For the tensor currents T and AT we use $\gamma_j \gamma_0 \otimes \gamma_j \gamma_0$ and $\gamma_i \gamma_k \otimes \gamma_i \gamma_k$ respectively, with i and k chosen as spatial directions and $i \neq k$. Note that we use the local currents to avoid tree-level discretization errors. The valence charm and heavy-quark masses used in this work are given in Table II, with $am_h = 0.9 \approx am_b$ on set 3 and $am_h = 0.625 \approx am_b$ on set 4. Note that because we use the HISQ formalism for both heavy and charm quarks, we can use $u = m_c^{\text{val}}/m_h^{\text{val}}$ directly. The ensembles we use include physically tuned charm and strange quarks in the sea, as

TABLE II. Details of the charm and heavy valence masses.

Set	am_h^{val}	am_c^{val}
1	0.5, 0.55, 0.6, 0.65, 0.7, 0.75, 0.8	0.449
2	0.427, 0.525, 0.55, 0.6, 0.65, 0.7, 0.75, 0.8	0.274
3	0.25, 0.3, 0.35, 0.4, 0.45, 0.5, 0.55, 0.6, 0.65, 0.7, 0.75, 0.8, 0.85, 0.9	0.194
4	0.2, 0.25, 0.3, 0.45, 0.625	0.137
5	0.5, 0.55, 0.6, 0.65, 0.7, 0.75, 0.8	0.433

well as unphysically heavy light sea quarks on sets 1–4. While the effect of using heavier-than-physical light quarks is expected to be very small, we also include a single ensemble, set 5, with physically tuned light quarks, in order to constrain these effects.

The Z_V factors for the local vector current were computed in [18,28], extrapolated to zero valence quark mass. For the tensor, we use the results of [29], which used an intermediate RI-SMOM scheme to match the lattice tensor current to the continuum tensor current in the $\overline{\text{MS}}$ scheme. We use the values computed using a matching scale of $\mu = 2$ GeV which we subsequently run to $\bar{m}_h(\bar{m}_h)$ using the three-loop anomalous dimension [30]. For HISQ, chiral symmetry means that the local vector and tensor currents used here have the same renormalization factors in the zero valence quark mass limit as their axial counterparts to all orders in perturbation theory [31]. It was shown in [28] that Z_V computed using the RI-SMOM scheme is free from condensate contamination, while Z_T includes a correction to remove condensate contributions explicitly [29]. We may therefore use $Z_A = Z_V$ and $Z_{AT} = Z_T$, which will differ only by discretization effects, and so give the correct continuum limit. The values of Z_V and Z_T used here are given in Table III. For each value of am_h on each ensemble, we run Z_T to the $\overline{\text{MS}}$ mass $\bar{m}_h(\mu = \bar{m}_h)$ which we determine using the physical value of $\bar{m}_c(3 \text{ GeV}) = 0.9858(51)$ GeV from [18] together with the ratio of lattice masses

$$\bar{m}_h(3 \text{ GeV}) = \bar{m}_c(3 \text{ GeV})/u = \bar{m}_c(3 \text{ GeV})/(am_c/am_h). \quad (17)$$

Note that since [29] did not include set 4, we use a value here obtained by extrapolating the other values. Following [18], we fit the condensate-corrected tensor renormalization factors, at scale $\mu = 2$ GeV, using the simple fit function

$$Z_T(a, \mu = 2 \text{ GeV}) = \sum_{i=0}^{i=4} \left(c_i + \sum_{j=1}^{j=3} b_{ij} \left(\frac{a\mu}{\pi} \right)^{2j} \right) \alpha_s(\pi/a)^i \quad (18)$$

TABLE III. The second column gives the values of $Z_V(\mu = 2 \text{ GeV})$ at zero valence quark mass computed in [18,28] in the RI-SMOM scheme. Note that Z_V on set 5 is equal to that on set 1. The third column gives the values of $Z_T(\mu = 4.8 \text{ GeV})$ from [29] for the tensor operators used in this work. Note that since [29] did not include set 4, we use a value here obtained by extrapolating the other values in a^2 as described in the text.

Set	$Z_V(\mu = 2 \text{ GeV})$	$Z_T(\mu = 4.8 \text{ GeV})$
1	0.98445(11)	1.0029(43)
2	0.99090(36)	1.0342(43)
3	0.99203(108)	1.0476(42)
4	0.99296(21)	1.0570(50)
5	0.98445(11)	1.0029(43)

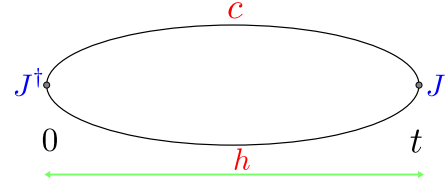


FIG. 1. Arrangement of heavy and charm quark propagators for currents $J = j^S, j^P, j^V, j^A, j^T, j^{AT}$ defined in Sec. II.

taking priors of 0 ± 2 for the coefficients c_i and b_{ij} . Varying either μ or the lattice scale, π/a , by $\pm 50\%$ has a negligible effect on the extrapolated value, as does increasing the maximum order that we sum to in i or j . Note that we neglect the statistical correlations between Z_V and Z_T as well as between the current renormalization factors and the lattice data generated in this work.

We use random wall sources to increase statistical precision. The arrangement of propagators appearing in the correlation functions which we compute are shown in Fig. 1. In terms of the staggered fields they are given by

$$C_\delta^{\text{latt}} = \frac{1}{L^3} \sum_{x,y,y'} \beta_\delta(x) g_{ab}^c(t, x; 0, y) \beta_\delta(y) \xi_{bc}(y) \times (g_{ad}^h(t, x; 0, y') \xi_{dc}(y'))^* \quad (19)$$

where g^q is the staggered propagator for flavor q and the random wall ξ satisfies $\xi_{ac}(y) \xi_{bc}^*(y') = \delta_{y,y'} \delta_{ab} \cdot \beta_\delta(x)$ is the x -dependent phase factor corresponding to the local spin-taste operator in the staggered formalism.

The correlation functions we compute are periodic in time, and so we average $C^{\text{latt}}(t)$ and $C^{\text{latt}}(L_t - t)$ for $0 < t < L_t/2$. We compute the time moments in Eq. (16) on the lattice as

$$\begin{aligned} \chi_{1^+}^{\text{latt}}(q^2 = 0) &= \frac{1}{12} \sum_{t=0}^{L_T/2} t^4 C_A^{\text{latt}}(t), \\ \chi_{1^-}^{\text{latt}}(q^2 = 0) &= \frac{1}{12} \sum_{t=0}^{L_T/2} t^4 C_V^{\text{latt}}(t), \\ \chi_{0^-}^{\text{latt}}(q^2 = 0) &= \frac{1}{12} (m_h + m_c)^2 \sum_{t=0}^{L_T/2} t^4 C_P^{\text{latt}}(t), \\ \chi_{0^+}^{\text{latt}}(q^2 = 0) &= \frac{1}{12} (m_h - m_c)^2 \sum_{t=0}^{L_T/2} t^4 C_S^{\text{latt}}(t), \\ \chi_{(A)T}^{\text{latt}}(q^2 = 0) &= \frac{1}{12} \sum_{t=0}^{L_T/2} t^4 C_{(A)T}^{\text{latt}}(t). \end{aligned} \quad (20)$$

The resulting values of $\chi_\delta^{\text{latt}}(q^2 = 0)$ for the (pseudo)scalar, (axial-)vector, and (axial-)tensor susceptibilities are given in Appendix A. The susceptibilities on a given ensemble are computed including all statistical correlations, which

are then included in our subsequent chiral continuum extrapolation. We use the GVAR [32] Python package to propagate uncertainties from our correlation functions to the susceptibilities and masses while maintaining correlations.

IV. CONTINUUM EXTRAPOLATION

In order to reach the continuum we fit the lattice susceptibilities against a form including dependence on u , am_h , am_c and the quark mass mistunings. We use the fit functions

$$\begin{aligned}\chi_{1^\pm}^{\text{latt}} &= \frac{1}{\bar{m}_h(\bar{m}_h)^2} \sum_{n=0}^{12} \bar{a}_n^{1^\pm} (1-u)^n \Delta_n^{1^\pm} \mathcal{N}_n^{1^\pm}, \\ \chi_{(A)T}^{\text{latt}} &= \frac{1}{\bar{m}_h(\bar{m}_h)^2} \sum_{n=0}^{12} \bar{a}_n^{(A)T} (1-u)^n \Delta_n^{(A)T} \mathcal{N}_n^{(A)T}, \\ \chi_{0^\mp}^{\text{latt}} &= (1 \pm u)^2 \sum_{n=0}^{12} \bar{a}_n^{0^\mp} (1-u)^n \Delta_n^{0^\mp} \mathcal{N}_n^{0^\mp},\end{aligned}\quad (21)$$

where as well as including constant terms, \bar{a}_n^δ also allows for scale dependence through α_s , as well as condensate contributions,

$$\bar{a}_n^\delta = a_n^\delta \times \left(1 + \beta_n^\delta \alpha_s(\bar{m}_h) + \kappa_n^\delta \frac{\langle \frac{\alpha_s}{\pi} G^2 \rangle}{\bar{m}_h^3 \bar{m}_c} \right) \quad (22)$$

where the $\bar{m}_h^3 \bar{m}_c$ factor was chosen to interpolate the expected quark mass dependence in both the $m_h \rightarrow m_b$ and $m_h \rightarrow m_c$ limits. We take $\langle \frac{\alpha_s}{\pi} G^2 \rangle = 0.02 \text{ GeV}^4$ and use Gaussian priors of $0(2)$ for β_n^δ and κ_n^δ .

Δ_n^δ parametrizes discretization effects as

$$\begin{aligned}\Delta_n^\delta &= 1 + \sum_{j=1}^6 b_{j,n}^\delta (am_h)^{2j} + \sum_{j=1}^6 c_{j,n}^\delta (am_c)^{2j} \\ &\quad + \tilde{b}_n^\delta (am_h)^2 \log(am_h) + \tilde{c}_n^\delta (am_c)^2 \log(am_c).\end{aligned}\quad (23)$$

We include terms accounting for log-enhanced discretization effects which, due to the tree-level improvement of the HISQ action, are expected to enter at $\mathcal{O}(\alpha_s)$ [33]. We take Gaussian priors of $0(2)$ for \tilde{b}_n^δ and \tilde{c}_n^δ .

Because our simulation is done using staggered quarks, the correlation functions contain a time-oscillating contribution from time-doubled states with opposite parity [21], with

$$C_\delta^{\text{latt}}(t) = \sum_n |\lambda_n^\delta|^2 e^{-E_n^\delta t} - (-1)^t |\lambda_n^{\delta, \text{osc}}|^2 e^{-E_n^{\delta, \text{osc}} t}. \quad (24)$$

When we perform the sums over t in Eq. (20), the oscillating state contribution gives zero up to discretization effects. For the $J^P = 0^-, 1^-$ and tensor currents, we expect

the oscillating states to have $E_n^{\text{osc}} > E_n$. In this case, the discretization effects due to the oscillating state contribution are highly suppressed relative to the nonoscillating ground state. For the $J^P = 0^+, 1^+$, and axial-tensor currents, however, we expect $E_n^{\text{osc}} < E_n$. In this case we can use the ground state parameters $\lambda_0^{(\text{osc})}$ and $E_0^{(\text{osc})}$, extracted from fits to Eq. (24) using the Python package CORRFITTER [34], to estimate the size of the discretization effects from the oscillating state contribution to Eq. (20) relative to the nonoscillating ground state contribution. We find that this discretization effect is expected to be largest on sets 1 and 5, at the level of approximately -15% , -5% , and -10% for $\chi_{1^+}^{\text{latt}}$, $\chi_{0^+}^{\text{latt}}$, and χ_{AT}^{latt} respectively. We therefore use a power series in $am_{q=h,c}$, as opposed to the more usual am_q/π , to capture these large discretization effects, including up to $(am_q)^{12}$. For $b_{j,n}^\delta$ and $c_{j,n}^\delta$, we use Gaussian priors of $0(2)$.

In [11] it is observed that the expansion up to $\mathcal{O}((1-u)^8)$ is indistinguishable from the full expressions for the leading order terms $\tilde{C}_1^{(0),\delta}(u)$ from $u = 0.8$ down to $u = u_{\text{phys}}$. The expansion up to $\mathcal{O}((1-u)^9)$ is also seen to reproduce the NLO and NNLO results well across the range $0.3 \leq u \leq 0.8$ with deviations of $\approx 10\%$ close to $u = u_{\text{phys}}$. Motivated by these observations, we include up to $(1-u)^{12}$ in our fit function. We have confirmed that this fit function reproduces the perturbative continuum results of [12] to 1 part in 10^6 across the range $u_{\text{phys}} \leq u \leq 0.8$, with all $|a_n^\delta| < 0.01$. As such we use conservative Gaussian priors of $0.0(0.05)$ for each a_n^δ for terms with $n \leq 8$ and $0.0(0.025)$ for terms with $n > 8$, reflecting that these terms are only needed to capture the NLO and NNLO u dependence of the perturbative results. \mathcal{N}^δ accounts for valence and quark mass mistuning effects,

$$\begin{aligned}\mathcal{N}_n^{\delta=1^\pm, (A)T} &= (1 + A^\delta \delta_{m_c}^{\text{val}}) (1 + B_n^\delta \delta_{m_c}^{\text{sea}} + C_n^\delta \delta_{m_s}^{\text{sea}} + D_n^\delta \delta_{m_l}^{\text{sea}}), \\ \mathcal{N}_n^{\delta=0^\pm} &= (1 + B_n^\delta \delta_{m_c}^{\text{sea}} + C_n^\delta \delta_{m_s}^{\text{sea}} + D_n^\delta \delta_{m_l}^{\text{sea}})\end{aligned}\quad (25)$$

with

$$\begin{aligned}\delta_{m_c}^{\text{val}} &= (am_c^{\text{val}} - am_c^{\text{tuned}}) / am_c^{\text{tuned}}, \\ \delta_{m_c}^{\text{sea}} &= (am_c^{\text{sea}} - am_c^{\text{val}}) / am_c^{\text{val}}, \\ \delta_{m_s}^{\text{sea}} &= (am_s^{\text{sea}} - am_s^{\text{tuned}}) / (10am_s^{\text{tuned}}), \\ \delta_{m_l}^{\text{sea}} &= (am_l^{\text{sea}} - am_s^{\text{tuned}} / [m_s/m_l]_{\text{phys}}) / (10am_s^{\text{tuned}}),\end{aligned}\quad (26)$$

and with $[m_s/m_l]_{\text{phys}} = 27.18(10)$ from [27]. When $m_c^{\text{val}} = m_c^{\text{sea}}$ the perturbative expressions for the susceptibilities are functions of only u , \bar{m}_h and $\alpha_s(\bar{m}_h)$. Charm quark mistuning effects thus enter our calculation through the determination of $\bar{m}_h(\bar{m}_h)$ using the physical value of $\bar{m}_c(3 \text{ GeV})$, as well as indirectly through the scale $\mu = \bar{m}_h$. The valence charm masses used here are well tuned, and the effect of the

TABLE IV. η_c masses in lattice units, used to determine am_c^{tuned} .

Set	aM_{η_c}
1	1.364965(66)
2	0.896644(80)
3	0.666886(75)
4	0.49423(16)
5	1.33045(97)

small mistuning on $\bar{m}_h(\bar{m}_h)$ leads to a negligible change in $\alpha_s(\bar{m}_h)$. Since the nonperturbative condensate contributions are expected to be small relative to the perturbative expressions, we also neglect their variation with the small valence charm mass mistunings. The only remaining place where mistuning effects may have a significant effect is the overall $1/\bar{m}_h^2$ appearing for the cases $\delta = 1^\pm, (A)T$. For these cases, we take $\mathcal{N}_n^{\delta=1^\pm, (A)T}$ to contain only a single overall $\delta_{m_c}^{\text{val}}$ factor. The relevant sea charm quark mistuning, which we denote $\delta_{m_c}^{\text{sea}}$, is then the mistuning of the sea charm quark mass from the valence mass m_c^{val} .

The tuned values of the quark masses are given by

$$am_c^{\text{tuned}} = am_c^{\text{val}} \frac{M_{\eta_c}^{\text{phys,QCD}}}{M_{\eta_c}}, \quad (27)$$

where we use the pure QCD result $M_{\eta_c}^{\text{phys,QCD}} = 2.9783(11)$ GeV, computed using the results of [18] for the J/ψ hyperfine splitting in pure QCD and neglecting disconnected diagrams as we do here. To determine M_{η_c} , we generate η_c correlation functions using local $\gamma^5 \otimes \gamma^5$ spin-taste operators, using the valence charm masses given in Table II. We fit these correlation functions to

$$C_{\eta_c}^{\text{latt}}(t) = \sum_{n=0}^{N_{\text{exp}}=8} |\lambda_n|^2 e^{-M_n t}, \quad (28)$$

taking heuristic Gaussian priors of 0(0.75) for $\lambda_{n>0}$, 0.25(0.125) for λ_0 , 0.75(0.6) GeV for $M_{n+1} - M_n$, and 3.0(0.75) GeV for $M_0 = M_{\eta_c}$. The values of M_{η_c} resulting from this fit are given in lattice units in Table IV, where we see excellent agreement with the values determined in [18], allowing for the small differences in valence masses on sets 1 and 4.

We take

$$am_s^{\text{tuned}} = am_s^{\text{val}} \left(\frac{M_{\eta_s}^{\text{phys}}}{M_{\eta_s}} \right)^2, \quad (29)$$

where we use the values of M_{η_s} given in [35]. Since these values are very precise, and since we expect sea quark mass mistuning effects to be small, we neglect their correlations with our other data. We take priors of 0(2) for each

$A^{\delta=1^\pm, (A)T}$, and 0.0(0.5) for C_n and D_n to reflect the fact that the corresponding sea quark mistuning effects appear at next-to-leading order in α_s . We take a prior of 0(0.1) for B_n , to reflect the results of the analysis of sea charm quark mistuning effects on w_0 in [15].

V. RESULTS

We use the Python package LSQFIT [36] to perform the fit to Eq. (21). Our lattice data points and continuum extrapolated susceptibilities for the (pseudo)scalar and (axial-)vector susceptibilities are plotted in Figs. 2 and 3. Our lattice data points for the tensor susceptibilities are shown in Fig. 4, together with the result of our chiral continuum extrapolation. The fit has $\chi^2/\text{dof} = 0.89$, which we estimate using singular value decomposition and prior noise [37], and a corresponding Q -value of $Q = 0.89$. We see that the discretization effects are visibly larger for χ_{1^+} as expected (see Sec. IV).

We find, for the physical b -quark,

$$\begin{aligned} \bar{m}_b^2 \times \chi_{1^+} &= 0.720(34) \times 10^{-2}, \\ \bar{m}_b^2 \times \chi_{1^-} &= 1.161(54) \times 10^{-2}, \\ \chi_{0^-} &= 2.374(33) \times 10^{-2}, \\ \chi_{0^+} &= 0.609(14) \times 10^{-2}, \end{aligned} \quad (30)$$

and for the tensor susceptibilities,

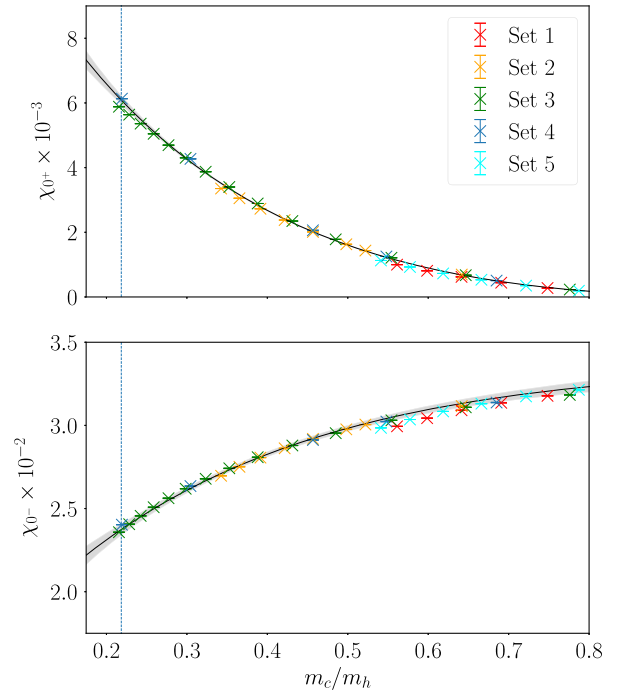


FIG. 2. Plot showing our lattice data points for the (pseudo)scalar susceptibilities, together with the result of our chiral continuum extrapolation (gray band) as a function of m_c/m_h for the (pseudo)scalar susceptibilities.

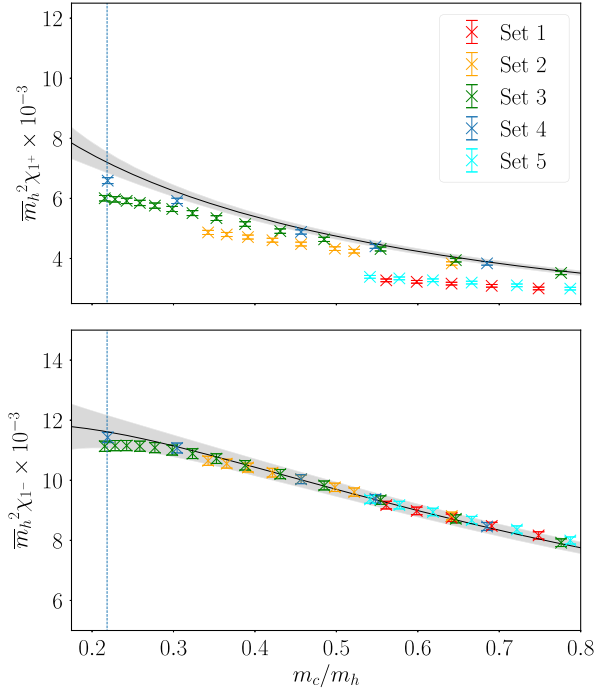


FIG. 3. Plot showing our lattice data points for the (axial-)vector susceptibilities, together with the result of our chiral continuum extrapolation (gray band) as a function of m_c/m_h for the (axial-)vector susceptibilities.

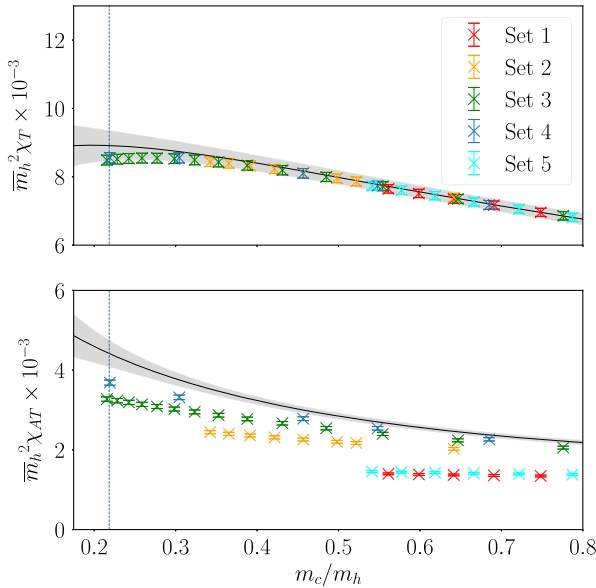


FIG. 4. Plot showing our lattice data points together with the result of our chiral continuum extrapolation (gray band) as a function of m_c/m_h for the (axial-)tensor susceptibilities. Note that the discretization effects appearing in the axial-tensor susceptibility are somewhat larger than expected from the estimate using ground state parameters extracted from correlator fits.

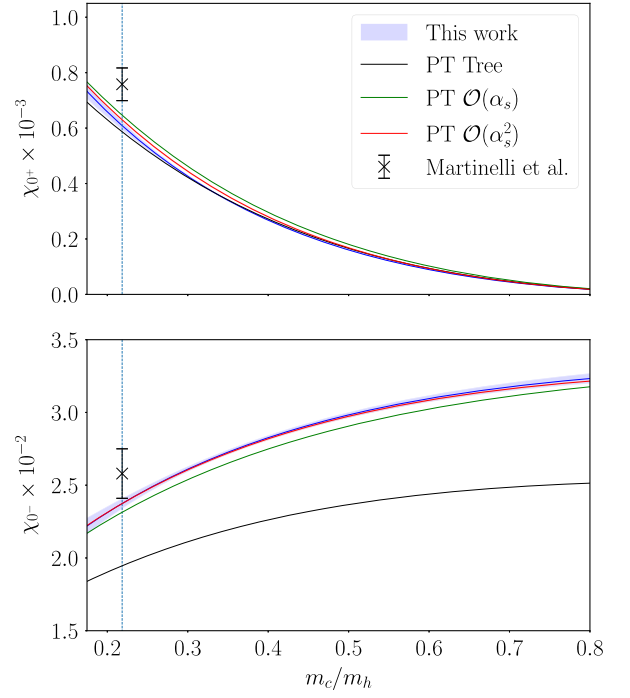


FIG. 5. Our chiral continuum fit results for the (pseudo)scalar susceptibilities (blue band) compared to the perturbative result at tree level (black line), $\mathcal{O}(\alpha_s)$ (green line) and $\mathcal{O}(\alpha_s^2)$ (red line). We add the leading condensate contribution from [9] to the $\mathcal{O}(\alpha_s^2)$ result in red, though this has a very small effect. The red band showing the uncertainty on the $\mathcal{O}(\alpha_s^2)$ result is equal to $(\alpha_s/\pi)^3$ multiplied by the root mean square of the three known coefficients. We also include the results of [13] for comparison. We see that our results are very close to the perturbation theory across the full range of m_c/m_h considered.

$$\begin{aligned} \bar{m}_b^2 \times \chi_T &= 0.891(44) \times 10^{-2}, \\ \bar{m}_b^2 \times \chi_{AT} &= 0.441(33) \times 10^{-2}. \end{aligned} \quad (31)$$

For ease of comparison to other results, we also give the (axial-)vector and (axial-)tensor susceptibilities with the factor of $1/\bar{m}_b^2$ included. We find

$$\begin{aligned} \chi_{1+} &= 4.06(20) \times 10^{-4} \text{ GeV}^{-2}, \\ \chi_{1-} &= 6.55(31) \times 10^{-4} \text{ GeV}^{-2}, \\ \chi_T &= 5.03(25) \times 10^{-4} \text{ GeV}^{-2}, \\ \chi_{AT} &= 2.49(19) \times 10^{-4} \text{ GeV}^{-2}. \end{aligned} \quad (32)$$

In order to provide self-contained results, we generate synthetic data across the full range of u between 0.8 and m_c/m_b and fit this data using a simple power series in $1 - u$ up to $(1 - u)^{12}$, as in Eq. (21), without any factors of α_s and $\langle \frac{\alpha_s}{\pi} G^2 \rangle$. We find that the susceptibilities computed from the results of this fit are indistinguishable from our full results, and we provide the posterior distributions for the coefficients in the file `susceptibilities_u12.pydat` in the Supplemental Material [38], as well as the Python script `load_chi_u12.py`, which loads the correlated parameters

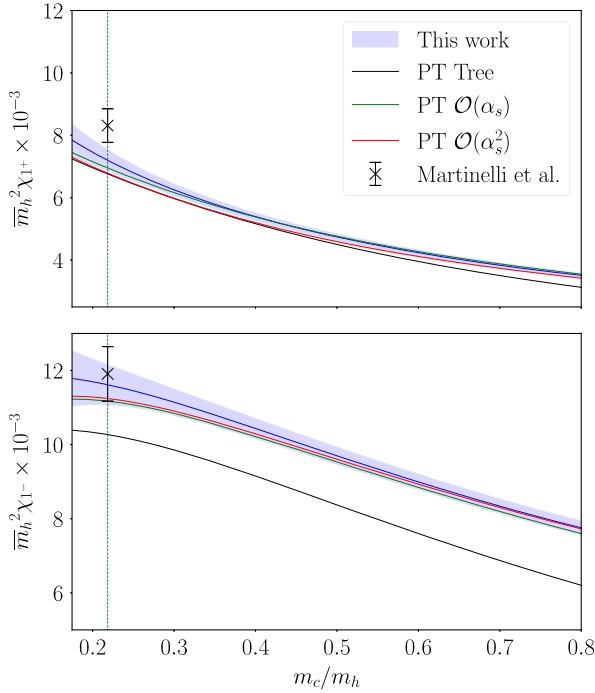


FIG. 6. Our chiral continuum fit results for the (axial-)vector susceptibilities (blue band) compared to the perturbative result at tree level (black line), $\mathcal{O}(\alpha_s)$ (green line), and $\mathcal{O}(\alpha_s^2)$ (red line). We add the leading condensate contribution from [9] to the $\mathcal{O}(\alpha_s^2)$ result in red, though this has a very small effect. The red band showing the uncertainty on the $\mathcal{O}(\alpha_s^2)$ result is equal to $(\alpha_s/\pi)^3$ multiplied by the root mean square of the three known coefficients. We also include the results of [13] for comparison. We see that our results are very close to the perturbation theory across the full range of m_c/m_h considered.

from susceptibilities_u12.pydat and computes the continuum susceptibilities.

A. Tests of the stability of the analysis

In order to demonstrate the robustness of our results to changes in the chiral continuum fit function Eq. (21), we repeat the above analysis for several variations of the fit function. We show results obtaining using fits with higher orders of $1 - u$ included, with higher orders in $am_{q=h,c}$ included, as well as a fit including only up to $(1 - u)^8$ and $(am_{q=h,c})^8$. In addition to these variations, we also show the results of fits excluding the $a^2 \log(a)$ terms from Eq. (23), as well as excluding the terms proportional to $\alpha_s(\bar{m}_h)$ and $(\frac{G}{\pi} G^2)$ in Eq. (22). The results of these fits are shown for $u = 0.2184$, $u = 0.5$, and $u = 0.8$ in Figs. 8–10 in Appendix B, where we see that our results vary only very slightly at each point for each different chiral continuum fitting strategy.

We also check that the effect of autocorrelations in simulation time is negligible by repeating our analysis using correlation functions which have been binned over every two configurations, as well as over every four configurations, on all ensembles. We find that in each case

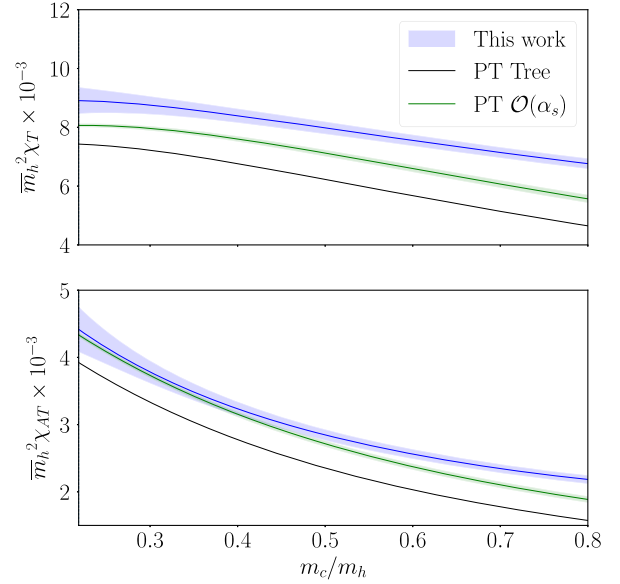


FIG. 7. Our chiral continuum fit results for the (axial-)tensor susceptibilities (blue band) compared to the perturbative result at tree level (black line) and $\mathcal{O}(\alpha_s)$ (green line) computed in [17]. The green band showing the uncertainty on the $\mathcal{O}(\alpha_s)$ result is equal to α_s^2 multiplied by the root mean square of the two known coefficients. We see that our results are in reasonable agreement for the axial-tensor susceptibility, but disagree for the tensor susceptibility.

the mean values of our results for the susceptibilities at $u = 0.2184$, $u = 0.5$, and $u = 0.8$ change by no more than 0.1σ , and the uncertainties change by at most 7%.

B. Comparison to existing results

The $\bar{b}c$ susceptibilities are expected to receive only extremely small nonperturbative condensate corrections, at the level of $\approx 0.05\%$ for the physical b -quark mass [9]. As such, we expect that there should be good agreement between our lattice results for the (pseudo)scalar and (axial-)vector susceptibilities and those determined using the results of [12].

Our continuum results for the (axial-)vector and (pseudo)scalar susceptibilities are plotted in Figs. 5 and 6, together with the LO, NLO, and NNLO results determined using the results of [12] that we describe in Sec. II. In addition to the NNLO perturbative result, we include the leading-order condensate contribution given in [9]. To evaluate these expressions, which are given in terms of the pole masses, we use the two-loop matching between the $\overline{\text{MS}}$ and pole masses from [39], allowing a 10% uncertainty for renormalon effects. We see that our lattice results, plotted as the blue band, are very close to the result including NNLO perturbation theory and leading condensate terms across the full range of u values considered. Taking each susceptibility in isolation, we find reasonable agreement between our results and the perturbation theory for the

vector, axial-vector, and pseudoscalar cases across the full range of u . Our result for the scalar susceptibility is in slight disagreement with the perturbative result in the region where $u \approx 0.3$.

The lattice results from [13] are also plotted in Figs. 5 and 6. We see good agreement between our results and those of [13] for χ_{1^-} , but disagreement at the level of $1 - 2\sigma$ for χ_{1^+} , χ_{0^-} , and χ_{0^+} . Note that we see good agreement between our results for χ_{0^-} , χ_{0^+} , χ_{1^-} , and χ_{1^+} and the preliminary results shown in [40].

For the (axial-)tensor cases, the susceptibilities have been computed perturbatively to $\mathcal{O}(\alpha_s)$ [17]. We plot our continuum results for the (axial-)tensor together with the perturbative results in Fig. 7. We see good agreement between our results and the perturbation theory for the axial-tensor susceptibility for $m_h \rightarrow m_b$, but poor agreement for $m_h \rightarrow m_c$. For the tensor susceptibility, we find significant disagreement with the NLO perturbative result across the full range of u .

VI. CONCLUSION

We have computed the full set of (pseudo)scalar, (axial-)vector, and (axial-)tensor susceptibilities, χ_{1^-} , χ_{1^+} , χ_{0^-} , χ_{0^+} , χ_T , and χ_{AT} , between $u = u_{\text{phys}}$ and $u = 0.8$, using the heavy-HISQ method, including up/down quarks, and physically tuned strange and charm quarks in the sea. Importantly, we include here a gauge field ensemble with $a \approx 0.03$ fm, sufficiently small for the physical b -quark mass to be reached, with $am_b \approx 0.625$.

We find that our results for the pseudoscalar and (axial-)vector susceptibilities are in agreement with the three-loop perturbation theory results [12], while the scalar susceptibility exhibits some tension. Our results demonstrate the reliability of this method of computing susceptibilities on the lattice. We find that the tensor and axial-tensor susceptibilities at the physical b -quark mass are roughly 1/3 smaller than the vector and axial-vector susceptibilities respectively. This is to be expected from the similar size difference seen in the OPE results for the $\bar{b}s$ tensor and axial tensor in [17] together with the observation that the fourth moments of the $\bar{h}s$ and $\bar{h}c$ correlators computed in [41] differ by only a few percent for the largest values of am_h . We find reasonable agreement with the NLO perturbation theory for the axial-tensor susceptibility, but for the tensor our results are in disagreement with the perturbative result, as seen in Fig. 7.

The results of this work will allow future lattice calculations of $b \rightarrow c$ form factors, for both mesonic and baryonic decays, to use dispersively bounded parametrizations for all form factors, for varying heavy quark mass between $1.25 \times m_c$ and m_b , using lattice results for all inputs. This work will also lead to future lattice calculations of less well-known quantities entering the dispersive bounds for other hadronic form factors, such as those needed for $b \rightarrow s$ decays [10] where perturbative

calculations of the susceptibilities are less reliable due to the much more sizeable condensate contributions.

ACKNOWLEDGMENTS

We are grateful to the MILC Collaboration for the use of their configurations and code. We thank C. T. H. Davies, C. Bouchar, C. McNeile, B. Colquhoun, D. van Dyk, M. Jung, and M. Bordone for useful discussions. Computing was done on the Cambridge service for Data Driven Discovery (CSD3), part of which is operated by the University of Cambridge Research Computing on behalf of the DIRAC HPC Facility of the Science and Technology Facilities Council (STFC). The DIRAC component of CSD3 was funded by BEIS capital funding via STFC capital Grants No. ST/P002307/1 and No. ST/R002452/1 and by STFC operations Grant No. ST/R00689X/1. DiRAC is part of the national e-infrastructure. We are grateful to the CSD3 support staff for assistance. Funding for this work came from UK Science and Technology Facilities Council Grants No. ST/L000466/1 and No. ST/P000746/1 and Engineering and Physical Sciences Research Council Project No. EP/W005395/1.

APPENDIX A: LATTICE DATA

Here we give our raw lattice results for the susceptibilities $\chi_\delta^{\text{latt}}(q^2 = 0)$ on each ensemble. Results for the (pseudo)scalar and (axial-)vector susceptibilities are given in Tables V–IX, while those for the (axial-)tensor currents are given in Tables X–XIV.

TABLE V. Susceptibilities χ_δ , defined in Eq. (20), for each value of am_h used on set 1.

am_h	$\chi_{1^+} \times 10^4 \text{ GeV}^2$	$\chi_{1^-} \times 10^4 \text{ GeV}^2$	$\chi_{0^-} \times 10^2$	$\chi_{0^+} \times 10^3$
0.55	28.99(44)	78.0(1.2)	3.2153(4)	0.13762(2)
0.6	30.02(44)	81.7(1.2)	3.1777(4)	0.27640(3)
0.65	30.90(45)	84.8(1.2)	3.1360(4)	0.44133(4)
0.7	31.63(45)	87.5(1.2)	3.0910(3)	0.62176(6)
0.75	32.23(45)	89.8(1.3)	3.0436(3)	0.80977(7)
0.8	32.72(45)	91.7(1.3)	2.9944(3)	0.99950(8)

TABLE VI. Susceptibilities χ_δ , defined in Eq. (20), for each value of am_h used on set 2.

am_h	$\chi_{1^+} \times 10^4 \text{ GeV}^2$	$\chi_{1^-} \times 10^4 \text{ GeV}^2$	$\chi_{0^-} \times 10^2$	$\chi_{0^+} \times 10^3$
0.427	38.34(56)	88.1(1.3)	3.1158(5)	0.69297(9)
0.525	42.42(61)	96.1(1.4)	3.0050(4)	1.4349(1)
0.55	43.28(62)	97.7(1.4)	2.9763(4)	1.6290(2)
0.6	44.80(63)	100.4(1.4)	2.9190(4)	2.0113(2)
0.65	46.08(65)	102.5(1.4)	2.8623(4)	2.3793(2)
0.7	47.13(66)	104.2(1.5)	2.8063(3)	2.7275(2)
0.75	47.99(68)	105.5(1.5)	2.7512(3)	3.0527(2)
0.8	48.67(69)	106.5(1.5)	2.6971(3)	3.3532(2)

TABLE VII. Susceptibilities χ_δ , defined in Eq. (20), for each value of am_h used on set 3.

am_h	$\chi_{1^+} \times 10^4 \text{ GeV}^2$	$\chi_{1^-} \times 10^4 \text{ GeV}^2$	$\chi_{0^-} \times 10^2$	$\chi_{0^+} \times 10^3$
0.25	35.19(57)	79.2(1.3)	3.1833(8)	0.23015(5)
0.3	39.45(61)	87.2(1.4)	3.1088(7)	0.6733(1)
0.35	43.16(66)	93.4(1.4)	3.0306(6)	1.2119(2)
0.4	46.36(70)	98.3(1.5)	2.9534(5)	1.7818(2)
0.45	49.12(74)	102.1(1.5)	2.8792(4)	2.3478(3)
0.5	51.46(77)	105.0(1.6)	2.8087(4)	2.8909(3)
0.55	53.45(80)	107.2(1.6)	2.7420(4)	3.4008(3)
0.6	55.11(83)	108.9(1.6)	2.6789(3)	3.8724(3)
0.65	56.48(85)	110.1(1.7)	2.6192(3)	4.3037(3)
0.7	57.60(87)	110.9(1.7)	2.5623(3)	4.6945(3)
0.75	58.49(88)	111.4(1.7)	2.5080(2)	5.0460(3)
0.8	59.18(90)	111.6(1.7)	2.4560(2)	5.3597(3)
0.85	59.70(91)	111.5(1.7)	2.4060(2)	5.6379(3)
0.9	60.06(92)	111.3(1.7)	2.3578(2)	5.8829(3)

TABLE VIII. Susceptibilities χ_δ , defined in Eq. (20), for each value of am_h used on set 4.

am_h	$\chi_{1^+} \times 10^4 \text{ GeV}^2$	$\chi_{1^-} \times 10^4 \text{ GeV}^2$	$\chi_{0^-} \times 10^2$	$\chi_{0^+} \times 10^3$
0.2	38.37(59)	84.6(1.3)	3.138(1)	0.5065(1)
0.25	44.04(66)	93.8(1.4)	3.0231(9)	1.2515(3)
0.3	48.84(72)	100.4(1.5)	2.9122(8)	2.0614(4)
0.45	59.18(88)	110.8(1.6)	2.6354(5)	4.2698(6)
0.625	65.92(99)	114.3(1.7)	2.4031(3)	6.1319(5)

TABLE IX. Susceptibilities χ_δ , defined in Eq. (20), for each value of am_h used on set 5.

am_h	$\chi_{1^+} \times 10^4 \text{ GeV}^2$	$\chi_{1^-} \times 10^4 \text{ GeV}^2$	$\chi_{0^-} \times 10^2$	$\chi_{0^+} \times 10^3$
0.55	29.97(44)	80.0(1.2)	3.2141(2)	0.19143(1)
0.6	31.06(45)	83.6(1.2)	3.1742(2)	0.35010(2)
0.65	31.98(45)	86.8(1.2)	3.1306(2)	0.53221(3)
0.7	32.74(46)	89.5(1.2)	3.0841(2)	0.72738(3)
0.75	33.38(46)	91.7(1.3)	3.0355(2)	0.92792(4)
0.8	33.89(46)	93.6(1.3)	2.9853(2)	1.12822(5)

TABLE X. Tensor and axial-tensor susceptibilities χ_δ , defined in Eq. (20), for each value of am_h used on set 1.

am_h	$\chi_T \times 10^4 \text{ GeV}^2$	$\chi_{AT} \times 10^4 \text{ GeV}^2$
0.55	67.1(1.2)	13.31(23)
0.6	69.6(1.2)	13.45(23)
0.65	71.7(1.2)	13.57(23)
0.7	73.5(1.2)	13.70(23)
0.75	75.1(1.2)	13.84(23)
0.8	76.4(1.2)	13.99(23)

TABLE XI. Tensor and axial-tensor susceptibilities χ_δ , defined in Eq. (20), for each value of am_h used on set 2.

am_h	$\chi_T \times 10^4 \text{ GeV}^2$	$\chi_{AT} \times 10^4 \text{ GeV}^2$
0.427	73.9(1.2)	20.24(34)
0.525	78.6(1.3)	21.70(35)
0.55	79.5(1.3)	22.02(36)
0.6	81.1(1.3)	22.61(36)
0.65	82.3(1.3)	23.13(37)
0.7	83.2(1.3)	23.60(38)
0.75	83.9(1.3)	24.03(39)
0.8	84.4(1.4)	24.42(39)

TABLE XII. Tensor and axial-tensor susceptibilities χ_δ , defined in Eq. (20), for each value of am_h used on set 3.

am_h	$\chi_T \times 10^4 \text{ GeV}^2$	$\chi_{AT} \times 10^4 \text{ GeV}^2$
0.25	68.6(1.2)	20.57(37)
0.3	73.5(1.3)	22.39(38)
0.35	77.2(1.3)	24.01(40)
0.4	79.9(1.3)	25.43(42)
0.45	81.9(1.4)	26.68(44)
0.5	83.3(1.4)	27.76(46)
0.55	84.3(1.4)	28.70(47)
0.6	84.9(1.4)	29.52(49)
0.65	85.3(1.4)	30.23(50)
0.7	85.4(1.4)	30.86(51)
0.75	85.5(1.4)	31.41(52)
0.8	85.4(1.4)	31.90(53)
0.85	85.2(1.4)	32.34(54)
0.9	84.9(1.4)	32.74(55)

TABLE XIII. Tensor and axial-tensor susceptibilities χ_δ , defined in Eq. (20), for each value of am_h used on set 4.

am_h	$\chi_T \times 10^4 \text{ GeV}^2$	$\chi_{AT} \times 10^4 \text{ GeV}^2$
0.2	71.8(1.3)	22.64(41)
0.25	77.3(1.4)	25.40(45)
0.3	81.0(1.4)	27.81(48)
0.45	85.5(1.5)	33.17(57)
0.625	85.6(1.5)	36.87(64)

TABLE XIV. Tensor and axial-tensor susceptibilities χ_δ , defined in Eq. (20), for each value of am_h used on set 5.

am_h	$\chi_T \times 10^4 \text{ GeV}^2$	$\chi_{AT} \times 10^4 \text{ GeV}^2$
0.55	68.1(1.2)	13.78(23)
0.6	70.6(1.2)	13.95(23)
0.65	72.7(1.2)	14.11(23)
0.7	74.5(1.2)	14.26(23)
0.75	76.0(1.2)	14.42(23)
0.8	77.3(1.2)	14.59(23)

APPENDIX B: STABILITY PLOTS

Figures 8–10 show the values of the susceptibilities at $u = 0.2184$, $u = 0.5$, and $u = 0.8$ computed using the variations of the fit described in Sec. VA. We see that our results are insensitive to such variations in fitting strategy.

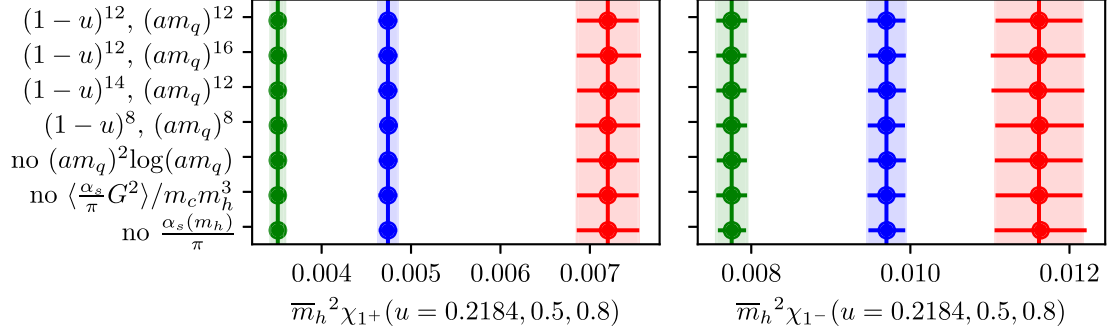


FIG. 8. Comparison of $\chi_{1-}(u)$ (left) and $\chi_{1+}(u)$ (right) at $u = 0.2184$ (red), $u = 0.5$ (blue), and $u = 0.8$ (green) computed using the variations of the fit described in Sec. VA, indicated on the vertical axis. The topmost value and filled band correspond to our final results. We see that our results vary only very slightly for these different methods of performing the extrapolation.

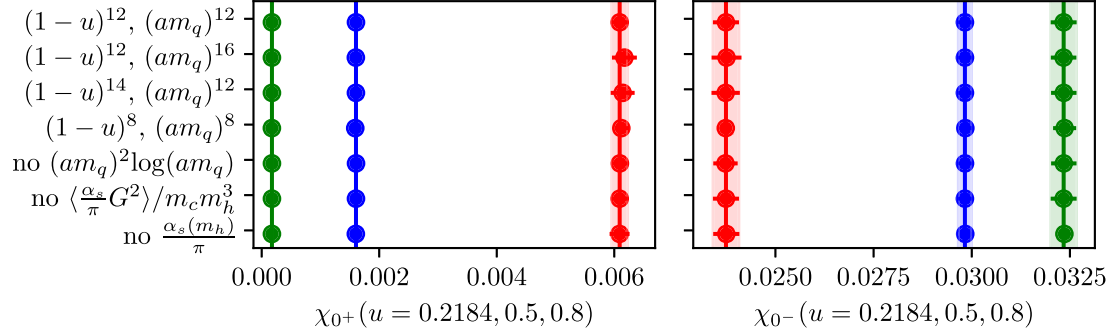


FIG. 9. Comparison of $\chi_{0-}(u)$ (left) and $\chi_{0+}(u)$ (right) at $u = 0.2184$ (red), $u = 0.5$ (blue), and $u = 0.8$ (green) computed using the variations of the fit described in Sec. VA, indicated on the vertical axis. The topmost value and filled band correspond to our final results. We see that our results vary only very slightly for these different methods of performing the extrapolation.

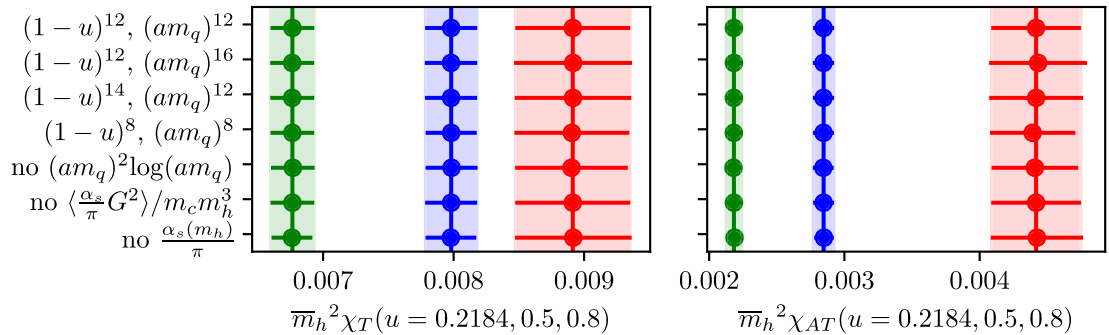


FIG. 10. Comparison of $\chi_T(u)$ (left) and $\chi_{AT}(u)$ (right) at $u = 0.2184$ (red), $u = 0.5$ (blue), and $u = 0.8$ (green) computed using the variations of the fit described in Sec. VA, indicated on the vertical axis. The topmost value and filled band correspond to our final results. We see that our results vary only very slightly for these different methods of performing the extrapolation.

- [1] A. Bazavov *et al.* (Fermilab Lattice and MILC Collaborations), *Eur. Phys. J. C* **82**, 1141 (2022); **83**, 21(E) (2023).
- [2] J. Harrison and C. T. H. Davies, *Phys. Rev. D* **109**, 094515 (2024).
- [3] Y. Aoki, B. Colquhoun, H. Fukaya, S. Hashimoto, T. Kaneko, R. Kellermann, J. Koponen, and E. Kou (JLQCD Collaboration), *Phys. Rev. D* **109**, 074503 (2024).
- [4] J. Harrison and C. T. H. Davies (HPQCD Collaboration), *Phys. Rev. D* **105**, 094506 (2022).
- [5] E. McLean, C. Davies, J. Koponen, and A. Lytle, *Phys. Rev. D* **101**, 074513 (2020).
- [6] J. Harrison, C. T. H. Davies, and A. Lytle (HPQCD Collaboration), *Phys. Rev. D* **102**, 094518 (2020).
- [7] E. Waheed *et al.* (Belle Collaboration), *Phys. Rev. D* **100**, 052007 (2019); **103**, 079901(E) (2021).
- [8] M. Bordone, N. Gubernari, D. van Dyk, and M. Jung, *Eur. Phys. J. C* **80**, 347 (2020).
- [9] C. Boyd, B. Grinstein, and R. F. Lebed, *Phys. Rev. D* **56**, 6895 (1997).
- [10] N. Gubernari, M. Reboud, D. van Dyk, and J. Virto, *J. High Energy Phys.* **12** (2023) 153.
- [11] J. Hoff and M. Steinhauser, *Nucl. Phys.* **B849**, 610 (2011).
- [12] J. Grigo, J. Hoff, P. Marquard, and M. Steinhauser, *Nucl. Phys.* **B864**, 580 (2012).
- [13] G. Martinelli, S. Simula, and L. Vittorio, *Phys. Rev. D* **104**, 094512 (2021).
- [14] I. Allison *et al.* (HPQCD Collaboration), *Phys. Rev. D* **78**, 054513 (2008).
- [15] B. Chakraborty, C. T. H. Davies, B. Galloway, P. Knecht, J. Koponen, G. C. Donald, R. J. Dowdall, G. P. Lepage, and C. McNeile, *Phys. Rev. D* **91**, 054508 (2015).
- [16] W. G. Parrott, C. Bouchard, and C. T. H. Davies (HPQCD Collaboration), *Phys. Rev. D* **107**, 014510 (2023).
- [17] A. Bharucha, T. Feldmann, and M. Wick, *J. High Energy Phys.* **09** (2010) 090.
- [18] D. Hatton, C. T. H. Davies, B. Galloway, J. Koponen, G. P. Lepage, and A. T. Lytle (HPQCD Collaboration), *Phys. Rev. D* **102**, 054511 (2020).
- [19] T. van Ritbergen, J. A. M. Vermaseren, and S. A. Larin, *Phys. Lett. B* **400**, 379 (1997).
- [20] D. Hatton, C. T. H. Davies, J. Koponen, G. P. Lepage, and A. T. Lytle, *Phys. Rev. D* **103**, 114508 (2021).
- [21] E. Follana, Q. Mason, C. Davies, K. Hornbostel, G. P. Lepage, J. Shigemitsu, H. Trotter, and K. Wong (HPQCD and UKQCD Collaborations), *Phys. Rev. D* **75**, 054502 (2007).
- [22] A. Bazavov *et al.* (MILC Collaboration), *Phys. Rev. D* **87**, 054505 (2013).
- [23] A. Bazavov *et al.* (MILC Collaboration), *Phys. Rev. D* **82**, 074501 (2010).
- [24] S. Borsanyi *et al.*, *J. High Energy Phys.* **09** (2012) 010.
- [25] R. J. Dowdall, C. T. H. Davies, G. P. Lepage, and C. McNeile, *Phys. Rev. D* **88**, 074504 (2013).
- [26] B. Chakraborty, C. T. H. Davies, P. G. de Oliveira, J. Koponen, G. P. Lepage, and R. S. Van de Water, *Phys. Rev. D* **96**, 034516 (2017).
- [27] A. Bazavov *et al.*, *Phys. Rev. D* **98**, 074512 (2018).
- [28] D. Hatton, C. Davies, G. Lepage, and A. Lytle (HPQCD Collaboration), *Phys. Rev. D* **100**, 114513 (2019).
- [29] D. Hatton, C. T. H. Davies, G. P. Lepage, and A. T. Lytle (HPQCD Collaboration), *Phys. Rev. D* **102**, 094509 (2020).
- [30] J. A. Gracey, *Phys. Lett. B* **488**, 175 (2000).
- [31] S. R. Sharpe and A. Patel, *Nucl. Phys.* **B417**, 307 (1994).
- [32] G. P. Lepage, GVAR Version 9.2.1, <http://github.com/gplepage/gvar>.
- [33] R. Sommer, L. Chimirri, and N. Husung, *Proc. Sci. LATTICE2022* (2023) 358 [arXiv:2211.15750].
- [34] G. P. Lepage, CORRFITTER Version 8.0.2, <http://github.com/gplepage/corrfitter>.
- [35] E. McLean, C. T. H. Davies, A. T. Lytle, and J. Koponen, *Phys. Rev. D* **99**, 114512 (2019).
- [36] G. P. Lepage, LSQFIT Version 11.4, <http://github.com/gplepage/lsqfit>.
- [37] R. Dowdall, C. Davies, R. Horgan, G. Lepage, C. Monahan, J. Shigemitsu, and M. Wingate, *Phys. Rev. D* **100**, 094508 (2019).
- [38] See Supplemental Material at <http://link.aps.org/supplemental/10.1103/PhysRevD.110.054506> for numerical results.
- [39] N. Gray, D. J. Broadhurst, W. Grafe, and K. Schilcher, *Z. Phys. C* **48**, 673 (1990).
- [40] A. Melis, F. Sanfilippo, and S. Simula, *Proc. Sci. LATTICE2023* (2024) 243 [arXiv:2401.03920].
- [41] C. T. H. Davies, K. Hornbostel, J. Komijani, J. Koponen, G. P. Lepage, A. T. Lytle, and C. McNeile (HPQCD Collaboration), *Phys. Rev. D* **100**, 034506 (2019).